PROCEEDINGS, 43rd Workshop on Geothermal Reservoir Engineering
Stanford University, Stanford, California, February 12-14, 2018
SGP-TR-213

Imaging Hydraulic Fracture Extents and Aperture Using Electrical Resistivity Tomography

Hui Wu, Pengcheng Fu, Xianjin Yang, Joseph P. Morris, and EGS Collab Team[1]

Atmospheric, Earth, and Energy Division, Lawrence Livermore National Laboratory, Livermore, CA 94550

Corresponding E-mail address: wu40@llnl.gov

Keywords: Electrical resistivity tomography, hydraulic fracture, extents, aperture, templated fracture inversion

ABSTRACT

Hydraulic fracturing has proven to be an essential technique to promote heat recovery in enhanced geothermal systems (EGS). A good understanding of fracture characteristics including its extents and aperture distribution plays an important role in the design and management of EGS. In the present study, we develop a new approach to use electrical resistivity tomography (ERT) to image the extents and aperture of a stimulated hydraulic fracture. This new method, named "templated fracture inversion", takes advantage of *a priori* known information about the host rock and the fracture to constrain the variable space for inversion. A series of inversions are performed on synthetic data based on designed sensor and fracture configuration in EGS Collab experiment 1. The results indicate that the algorithm is effective in inverting the fracture extents and aperture, both for conductive and (nearly) nonconductive fracture fluid as long as sufficient contrast in electric resistivity between the host rock and the fracture fluid is present. The templated inversion is more accurate and robust in imaging hydraulic fractures than the traditional smoothness constrained inversion method.

1. INTRODUCTION

Hydraulic fracturing create fracture network to improve the permeability of host rocks and has been used for recovering petroleum, natural gas and geothermal energy from subsurface reservoirs. Determining the extents and aperture distribution of the stimulated fracture is particularly important for the efficient exploitation and management of reservoir. The correct evaluation of the effect of hydraulic fracturing on surrounding formations and regional groundwater quality also largely depends on the accurate prediction of fracture extents, especially in the vertical direction (Davies et al. 2012; Fisher and Warpinski 2012; Vidic et al. 2013). Many methods have been developed to delineate the location and geometry of hydraulic fracture, including microseismic monitoring and tiltmeter arrays (Niitsuma and Saito 1991; Vinegar et al. 1992; Wills et al. 1992; Wright et al. 1995; Castillo et al. 1997; Maxwell et al. 2002; He et al. 2014; Maxwell 2014; Trowbridge et al. 2017). These methods can provide useful knowledge about the spatial extent of hydraulically induced fracture. However, there still remain some uncertainties in the interpretation of measurements from these methods (McClure and Horne 2014; Weiss et al. 2016). The occurrence of microseismic events is neither a necessary nor a sufficient condition of the presence of hydraulic fracture at that location. Tiltmeters usually cannot determine the full extents of a hydraulic fracture.

Electrical resistivity tomography (ERT) is a popular geophysical imaging technique which takes advantage of the spatial and temporal evolution of electrical resistivity distribution to image subsurface structure and process. Up to now, this technique has found its application in many subsurface engineering, such as water and salt infiltration, mineral exploration, thermal remediation, steam injection, geologic carbon sequestration, air sparging, aquifer characterization, and landfill leachate leakage (Daily et al. 1992; Ramirez et al. 1993; Lesur et al. 1999; Slater and Sandberg 2000; LaBrecque and Yang 2001; Doetsch et al. 2010; Coscia et al. 2011; Yang et al. 2014; Bouchedda et al. 2017). ERT has also been used for the detection of fractures in rock since the presence of fracture with electrically conductive or nonconductive fluids will change the distribution of electrical resistivity in the concerned rock mass (Slater et al. 1997; Nimmer et al. 2007; Magnusdottir and Horne 2011; Ramachandran et al. 2012; Robinson et al. 2013; Robinson et al. 2015; Robinson et al. 2016; Weiss et al. 2016). The imaging of fracture requires a significant electric conductivity contrast between the fracture and the surrounding matrix, especially for hydraulic fracture whose aperture might be too small to generate effective ERT measurements. However, previous ERT methodologies developed based on the Occam's inversion method always seek the solution with the least heterogeneities in electric conductivity distribution from the many solutions that fit the ERT measurements equally well. Therefore, the sharp electric conductivity contrast from either conductive or nonconductive fracture fluid is difficult to be correctly imaged with this kind of smoothness constrained inversion methods. In order to improve the cross-borehole ERT imaging of the sharp electric conductivity induced by subsurface structures such as fracture and clay layer, a method named "regularization disconnect" is proposed to remove the smoothness constraint along the structure boundaries by taking advantage of *a priori* known information about the structure location defined from borehole logging data (Slater and Binley 2006; Coscia et al. 2011; Johnson et al. 2012; Robert et al. 2012; Bazin and Pfaffhuber 2013; Robinson et al. 2013;

[1] J. Ajo-Franklin, S.J. Bauer, T. Baumgartner, K. Beckers, D. Blankenship, A. Bonneville, L. Boyd, S.T. Brown, J.A. Burghardt, T. Chen, Y. Chen, K. Condon, P.J. Cook, P.F. Dobson, T. Doe, C.A. Doughty, D. Elsworth, J. Feldman, A. Foris, L.P. Frash, Z. Frone, P. Fu, K. Gao, A. Ghassemi, H. Gudmundsdottir, Y. Guglielmi, G. Guthrie, B. Haimson, A. Hawkins, J. Heise, C.G. Herrick, M. Horn, R.N. Horne, J. Horner, M. Hu, H. Huang, L. Huang, K. Im, M. Ingraham, T.C. Johnson, B. Johnston, S. Karra, K. Kim, D.K. King, T. Kneafsey, H. Knox, J. Knox, D. Kumar, K. Kutun, M. Lee, K. Li, R. Lopez, M. Maceira, N. Makedonska, C. Marone, E. Mattson, M.W. McClure, J. McLennan, T. McLing, R.J. Mellors, E. Metcalfe, J. Miskimins, J.P. Morris, S. Nakagawa, G. Neupane, G. Newman, A. Nieto, C.M. Oldenburg, W. Pan, R. Pawar, P. Petrov, B. Pietzyk, R. Podgorney, Y. Polsky, S. Porse, S. Richard, M. Robertson, W. Roggenthen, J. Rutqvist, D. Rynders, H. Santos-Villalobos, P. Schwering, V. Sesetty, A. Singh, M.M. Smith, H. Sone, C.E. Strickland, J. Su, C. Ulrich, N. Uzunlar, A. Vachaparampil, C.A. Valladao, W. Vandermeer, G. Vandine, D. Vardiman, V.R. Vermeul, J.L. Wagoner, H.F. Wang, J. Weers, J. White, M.D. White, P. Winterfeld, T. Wood, H. Wu, Y.S. Wu, Y. Wu, Y. Zhang, Y.Q. Zhang, J. Zhou, Q. Zhou, M.D. Zoback

Robinson et al. 2015; Robinson et al. 2016). Results from this method indicated that utilizing *a priori* known information was important for reducing inversion artifacts and improve the imaging of sharp electric conductivity contrast presented by fractures.

Compared to other natural structures and fractures in the rock formation, the creating of hydraulic fracture is an artificially controlled process and useful *a priori* known information enables accurate ERT imaging of the fracture. The *a priori* known information includes: 1) electric conductivity distribution in matrix σ_m, which can be obtained by performing smoothness constrained inversion prior to hydraulic fracturing; 2) electric conductivity of fluid used in the stimulation σ_f; 3) likely location of the plane that hydraulic fractures will be stimulated, which can be estimated according to the local stress orientation and the position of well casing perforations; 4) likely fracture shape and its continuity. With such *a priori* known information, we only need to invert for the fracture boundary that interrupt the smoothness distribution of electric conductivity in matrix, rather than invert for the electric conductivity distribution in the whole matrix. Therefore, we develop a novel cross-borehole ERT method, named templated fracture inversion, to image both the extents and aperture distribution of hydraulic fracture. Instead of inverting for the distribution of electric conductivity, the variables describing the position, shape, size and aperture distribution of the fracture are inverted. In the following sections, we first describe the basic considerations and strategy for the templated fracture inversion method, including the inversion formulation. Based on a three-dimensional (3D) model simplified from the EGS Collab project design (Kneafsey et al., 2018; Morris et al., 2018), a series of inversions are then performed on synthetic data with different fracture configurations and aperture distributions to validate the capability of the method.

2. TEMPLATED FRACTURE INVERSION METHOD

The templated fracture inversion module is implemented in GEOS, a fully coupled hydraulic fracture simulation code developed at the Lawrence Livermore National Laboratory (Settgast et al. 2016). Similar to previous ERT inversion modules, the templated fracture inversion module includes both a forward model and an inversion model. The forward model is used to calculate electric potential distribution for a given electric conductivity (or resistivity) field and electrical boundary conditions. Fractures with different shape, size and aperture distribution can be considered in the forward model thanks to GEOS's fracture handling capability (Fu et al. 2013; Settgast et al. 2016). The finite volume method is used as the numerical framework in the forward model. The inversion model includes both the smoothness constrained inversion method and the templated fracture inversion method.

According to previous studies, the smoothness constrained inversion method attempts to determine the "best" distribution of the electric conductivity that presents the best fitness between the results calculated from the forward module and the measurements (Dey and Morrison 1979; Spitzer 1995; LaBrecque et al. 1999; LaBrecque and Yang 2001; Daily et al. 2005). To find the optimal distribution of the electric conductivity $\mathbf{P}$, the algorithm seeks to minimize the objective function consists of the L-2 norm of the data misfit and the stabilizing term that constrain the search of $\mathbf{P}$. The objective function can be expresses as,

$$\Psi(\mathbf{P}^*) = \chi^2(\mathbf{P}) + \alpha \mathbf{P}^{*T}\mathbf{R}\mathbf{P}^* = [\mathbf{D} - F(\mathbf{P}^*)]^T\mathbf{W}[\mathbf{D} - F(\mathbf{P}^*)] + \alpha \mathbf{P}^{*T}\mathbf{R}\mathbf{P}^* = 0 \quad (1)$$

where $\chi^2(\mathbf{P})$ denotes the Chi-squared statistics, $\mathbf{D}$ is the vector of electric potential measurements, $\mathbf{P}^*$ is the logarithm of $\mathbf{P}$, $F(\mathbf{P}^*)$ is the forward solution, $\mathbf{W}$ is the data-weight matrix, $\mathbf{R}$ is the roughness matrix, α is the weight factor of the roughness matrix. The non-diagonal elements of $\mathbf{W}$ are 0 and the diagonal elements are the reciprocals of the measurement variances. The roughness matrix $\mathbf{R}$ is expressed as $\mathbf{x}^T\mathbf{x} + \mathbf{y}^T\mathbf{y} + \mathbf{z}^T\mathbf{z}$, where $\mathbf{x}$, $\mathbf{y}$, and $\mathbf{z}$ are matrices first-order difference operators in the x, y and z directions. The weight factor α is estimated and updated according to the method used by LaBrecque et al. (1999).

The minimization of $\Psi(\mathbf{P}^*)$ requires that its derivative equals 0. Further employing the Newton's method, the following iterative equation can be obtained,

$$(\mathbf{A}_k^T\mathbf{W}\mathbf{A}_k + \alpha\mathbf{R})^T\Delta\mathbf{P}_k^* = [\mathbf{A}_k^T\mathbf{W}(\mathbf{D} - F(\mathbf{P}_k^*)) - \alpha\mathbf{R}\mathbf{P}_k^*] \quad (2)$$

where $\mathbf{A}_k$ is the sensitivity matrix at the kth iteration, $\mathbf{P}_k^*$ is the vector of the logarithm of electric conductivity from the previous iteration, $\Delta\mathbf{P}_k^*$ is the increment of $\mathbf{P}_k^*$ at the current iteration. The elements of the sensitivity matrix are calculated as $a_{i,j} = \partial F_i(\mathbf{P}_k^*)/\partial p_j$, where $F_i(\mathbf{P}_k^*)$ is the ith element of the forward solution and p_j is the jth element of $\mathbf{P}_k^*$. We used $\chi^2(\mathbf{P})$ equals to the number of measurements as the convergence criteria for the iteration.

For the templated fracture inversion method, the electric conductivity in the surrounding matrix is *a priori* known information, and the variable vector $\mathbf{V}$ consists of the parameters describing the fracture extents and aperture distribution. In the current study, we use an ellipse as the template for hydraulic fracture (Fig. 1), and the variables describing the fracture include the position of the fracture center (x_0, y_0), semi axis length (a, b), rotation angle (θ) and aperture (w). Note the coordinates here are on the 2D coordinate system on the *a priori* known fracture plane. The aperture w is described by the superposition of a series of functions w_i. For example, if we use the Gaussian function to describe the aperture distribution, the following expressions can be obtained,

$$w = \sum_{i=1}^{n} w_i + w_0 = \sum_{i=1}^{n} \frac{A_i}{\sqrt{2\pi}\,\varepsilon_i} e^{-\frac{(\mathbf{x}-\mathbf{x}_i)^2}{2\varepsilon_i^2}} + w_0 \quad (3)$$

where n is the number of Gaussian functions for the aperture distribution, w_0 is the base aperture, A_i and ε_i are parameters for the ith Gaussian function, $\mathbf{x}_i$ is the coordinates of the peak of the ith Gaussian function. The total length of the variable vector $\mathbf{V}$ for the templated fracture inversion is therefore $4n+6$. If n equals 0, the aperture is uniform in the fracture. Similar to the smoothness constrained inversion method, the following iteration equation can be obtained,

$$(\mathbf{S}_k^T\mathbf{W}\mathbf{S}_k)\Delta\mathbf{V}_k = \mathbf{S}_k^T\mathbf{W}(\mathbf{D} - F(\mathbf{V}_k)) \quad (4)$$

where $\mathbf{S}_k$ is the sensitivity matrix at the kth iteration, $\mathbf{V}_k$ is the variable vector from the previous iteration, $\Delta\mathbf{V}_k$ is the increment of $\mathbf{V}_k$ at the current iteration. The data-weight matrix $\mathbf{W}$ is the same as that in smoothness constrained inversion method. The iteration stops when the relative Chi-squared statistics (defined as the ratio between $\chi^2(\mathbf{V})$ at the current iteration and the first iteration) is smaller than 10^{-6}.

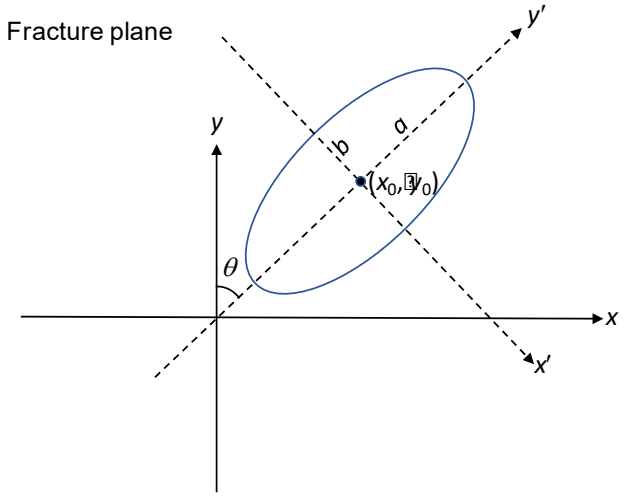

Figure 1: Elliptical fracture shape used for the templated fracture inversion method. Variables describing the fracture include the coordinates of the fracture center x_0, y_0, semi-major axis a, semi-minor axis b, rotation angle θ, and aperture w.

3. RESULTS

3.1 Model description

To verify the capability of the templated fracture inversion method for ERT imaging of hydraulic fracture, we develop a 3D model based on the Enhanced Geothermal Systems (EGS) Collab project, which is designed to investigate the hydraulic fracturing mechanics at a intermediate-scale coupled with geophysical monitoring such as optical/acoustic televiewer logging, seismic tomography and ERT (Huang et al. 2017; Knox et al. 2017). The Collab project's first experiment will be performed in the West Access Drift of the SURF facility at 4,850 feet below ground. A stimulation as well as a production well will be drilled in the minimum principal stress direction and hydraulic fractures with expected diameters of 20 to 30 m will be initialed to connect the two wells. Four monitoring boreholes parallel to the expected fracture planned have been drilled and geophysical monitoring equipment including electrodes used for ERT will be deployed in these boreholes. Based on the design of the Collab project's first experiment, a 500 × 500 × 300 m 3D domain is used to perform templated fracture inversion with electrode deployment consistent with the orientation of the four monitoring boreholes (Fig. 2). The expected fracture plane has $z = 0$, where the mesh resolution is 1 m in x and y direction, and 2 m in z direction. Fig. 2 (b) and (c) zoom in the model center to show a hypothetical fracture and the electrode layout.

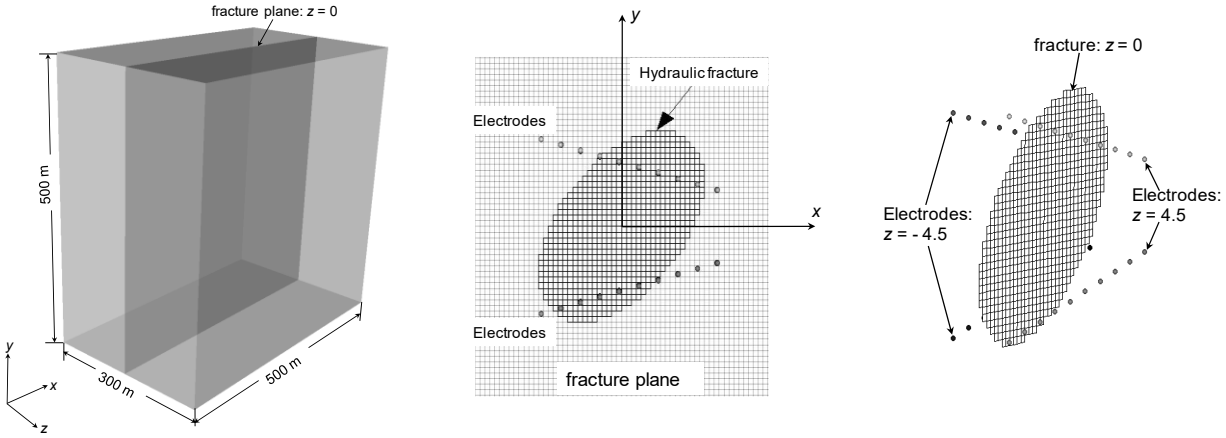

(a) (b) (c)

Figure 2: A 3D model for templated fracture inversion. (a) The 3D computational domain. A vertical hydraulic fracture is assumed to be stimulated in the fracture plane ($z = 0$). (b) A hypothetical elliptical hydraulic fracture near the center of the fracture plane. (c) The electrode deployment pattern. Totally four electrode arrays are deployed corresponding to the four monitoring boreholes drilled in the EGS Collab project. Two electrode arrays located in front of the fracture ($z = 4.5$ m),

and the other two electrode arrays are symmetrically on the back of the fracture (z = -4.5 m). Each array contains 10 electrodes with a 4.1 m spacing.

A series of templated fracture inversions are performed to verify its capability of imaging hydraulic fracture under different conditions, including more conductive and more nonconductive fracture fluid compared with that of the surrounding rock formation, as well as uniform and non-uniform aperture distributions. The effects of fracture mismatch (either in fracture extents or aperture distribution) is also analyzed. For each templated fracture inversion, a series of forward calculations are first performed to generate synthetic ERT measurements using dipole-dipole method. The model boundaries are assumed to be mixed boundaries for electrical current, which is appropriate to describe a far field boundary in ERT forward model (Dey and Morrison, 1979).

3.2 Imaging of fracture extents and aperture distribution

The first example uses an assumed elliptical fracture with a uniform aperture distribution (1 mm) to generate the synthetic data. The electric conductivity of surrounding rock formation σ_m in the model is uniform with a value of 0.001 S/m. Totally 1,140 ERT measurements are used for the templated fracture inversion process. The column in Fig. 3 shows the fractures as well as the aperture distribution in forward models. The other three columns show the fractures from inversion at different iterations, and the fracture extents in forward model is also plotted for comparison (illustrated as the black grid). Within 40 iterations, the fracture extents as well as aperture in the fracture can be determined with high accuracy, both for nonconductive and conductive fracture fluid scenarios.

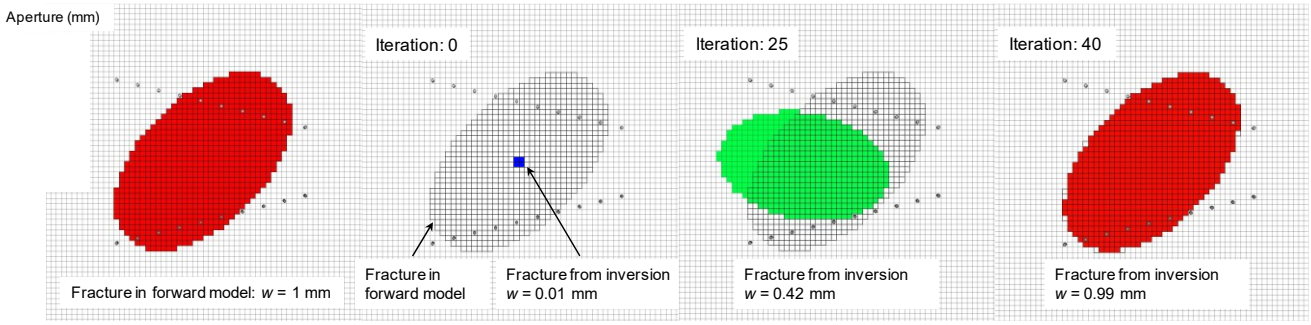

(a) Assuming fracture fluid is significantly less conductive than the host rock

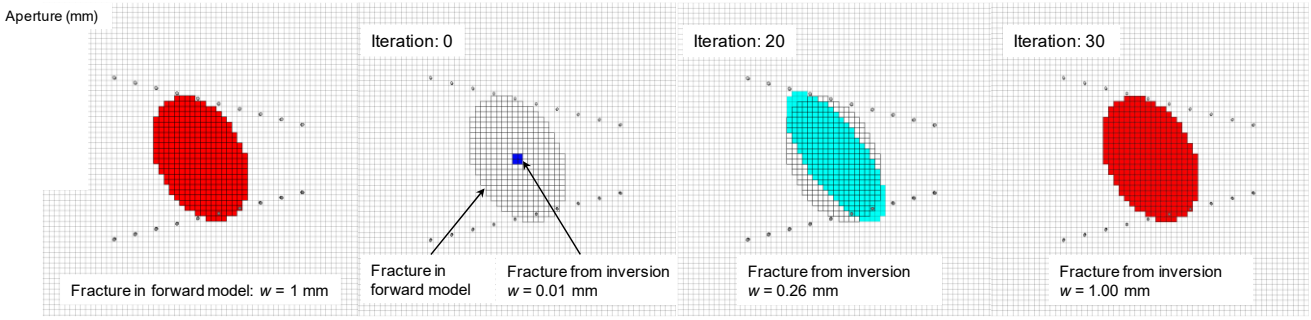

(b) Assuming fracture fluid is significantly more conductive than the host rock

Figure 3: Imaging of hydraulic fracture with uniform aperture distribution. (a) The parameters describing the elliptical fracture in forward model are x_0 = 0 m, y_0 = 0 m, a = 21.2 m, b = 12.7 m, θ = 45.0°, w = 1 mm, $\sigma_f = 1 \times 10^{-7}$ S/m. The starting fracture in the inversion model is denoted by the blue square at 0 iteration, with an initial aperture of 0.01 mm; (b) The parameters describing the elliptical fracture in forward model are x_0 = 0 m, y_0 = 0 m, a = 13.4 m, b = 8.9 m, θ = 26.6°, w = 1 mm, σ_f = 10 S/m. The starting fracture in the inversion model is denoted by the blue square at 0 iteration, with an initial aperture of 0.01 mm.

Fig. 4 displays the inversion results for an elliptical fracture with non-uniform aperture distribution, which is described by a Gaussian function as mentioned before. The distribution of σ_m is the same as that in Fig. 3, and also 1140 ERT measurements are used for the

inversion. According to the inversion results, the templated fracture inversion method first matches the fracture extents and then gradually matches the aperture distribution.

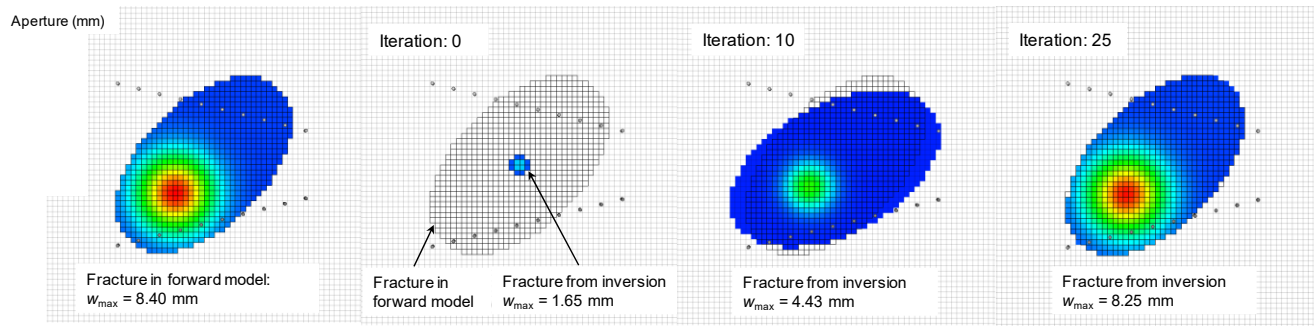

(a) Assuming fracture fluid is significantly less conductive than the host rock

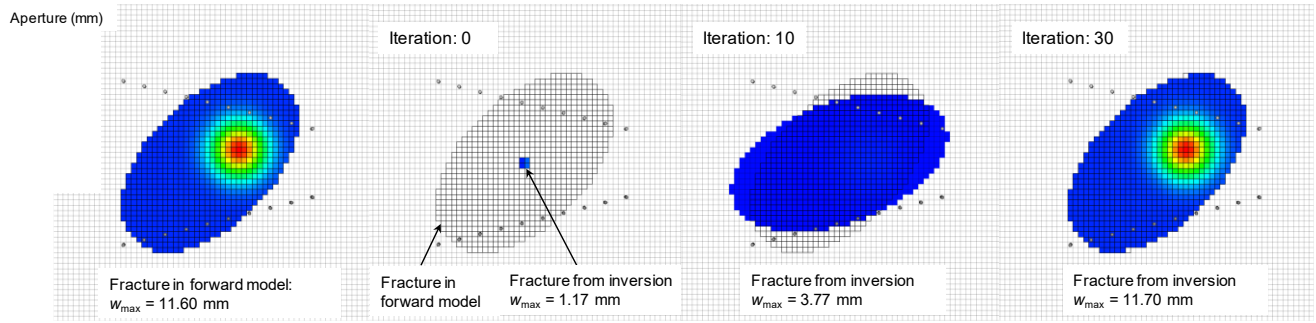

(b) Assuming fracture fluid is significantly more conductive than the host rock

Figure 4: Imaging of hydraulic fracture with non-uniform aperture distribution. (a) The parameters describing the elliptical fracture in forward model are x_0 = 0 m, y_0 = 0 m, a = 21.2 m, b = 12.7 m, θ = 45.0°, $\sigma_f = 1 \times 10^{-7}$ S/m. The parameters for the Gaussian function describing the aperture distribution are n = 1, $\mathbf{x}_1$ = (-5, -5, 0), A_1 = 0.1, ε_1 = 5.0, w_0 = 0.5 mm. The initial aperture distribution for the inversion process is also described by a Gaussian function with parameters n = 1, $\mathbf{x}_1$ = (0, 0, 0), A_1 = 0.005, ε_1 = 1.0, w_0 = 0.1 mm; (b) The parameters describing the elliptical fracture in forward model are the same as that for the nonconductive fracture fluid scenario, and σ_f = 10 S/m. The parameters for the Gaussian function describing the aperture distribution are n = 1, $\mathbf{x}_1$ = (6, 3, 0), A_1 = 0.1, ε_1 = 3.5, w_0 = 0.5 mm. The initial aperture distribution for the inversion process is also described by a Gaussian function with parameters n = 1, $\mathbf{x}_1$ = (1.5, 0, 0), A_1 = 0.005, ε_1 = 1.0, w_0 = 0.1 mm.

3.3 Comparison of templated fracture inversion and smoothness constrained inversion

In this section, both the traditional voxel-based, smoothness constrained inversion and templated inversion are performed on the same synthetic ERT measurements to compare their abilities for the imaging of hydraulic fracture. A circular hydraulic fracture with a uniform aperture distribution is assumed in the forward model and two different fracture locations are considered as shown in Fig. 5. Since the location of the plane that hydraulic fracture is stimulated is used as *a priori* known information, we only inverse the electric conductivity distribution on this fracture plane during smoothness constrained inversion, and the electric conductivity of the other elements in the model is fixed to the background value (the same as that used in the forward model). Totally 1140 ERT measurements are used for both the two inversion methods.

Fig. 5(a) shows the inversion results from smoothness constrained inversion method. The area with relative low electric conductivity (nonconductive fracture fluid condition) or high electric conductivity (conductive fracture fluid condition) can provide an estimate of the likely fracture area, however, part of the fracture area cannot be imaged especially when the fracture crosses the electrode arrays. In addition, the aperture distribution cannot be imaged using the smoothness constrained inversion method, and the artifacts near electrodes

may also cause some misinterpretation of the fracture extents. Fig. 5(b) displays the corresponding inversion results from the templated fracture inversion method. Both the fracture extents and aperture are correctly imaged.

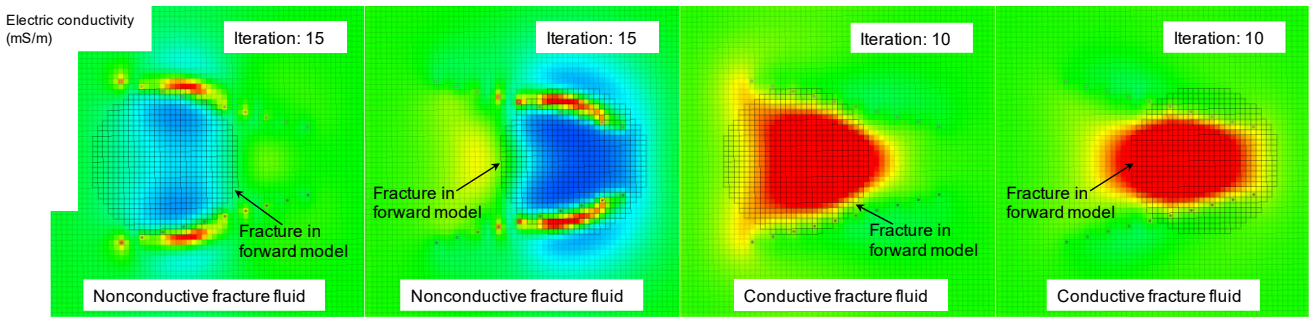

(a) Smoothness constrained inversion results

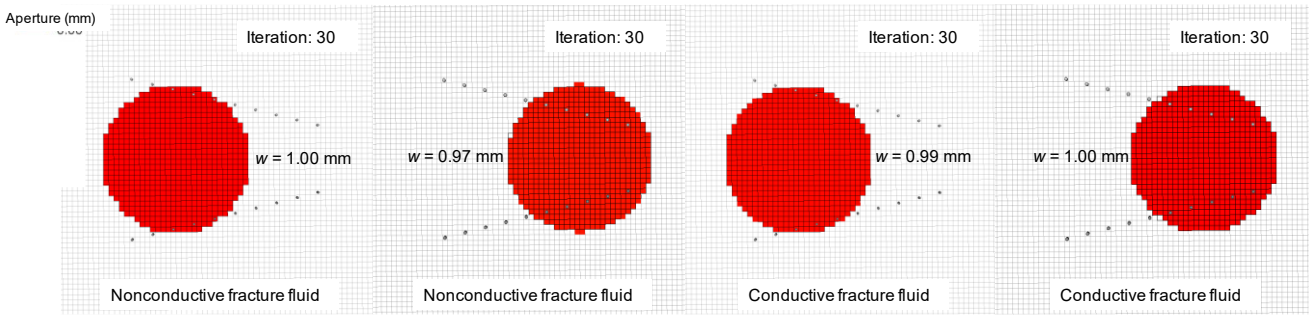

(b) Templated fracture inversion results

Figure 5: Comparison of smoothness constrained inversion and templated fracture inversion. (a): Parameters used in the forward model: fracture radius is 15 m, σ_m = 0.001 S/m, σ_f = 1 × 10^{-7} S/m (nonconductive fracture fluid condition) or 10 S/m (conductive fracture fluid condition), w = 1 mm. Parameters used for the starting model in the inversion process: fracture radius is 1 m, and σ_m = 0.001 S/m; (b) The forward model is the same as that used for the smoothness constrained inversion. Parameters used for the starting model in the inversion process: fracture radius is 1 m, σ_m = 0.001 S/m, σ_f = 1 × 10^{-7} S/m (nonconductive fracture fluid condition) or 10 S/m (conductive fracture fluid condition), initial aperture is 0.01 mm.

3.4 Mismatch between fracture characteristics and templates

In the above examples, the assumed fracture characteristics can be fully covered by the adopted template. In theory, the fracture extents and aperture distribution can be accurately matched in the forward and inversion model if no noise is presented in the ERT measurements (Figs. 3, 4 and 5(b)). However, the hydraulic fracture shape is generally irregular and the aperture distribution is also highly heterogeneous due to the complex geologic and operation conditions. As a result, there will always be a mismatch in fracture extents and aperture distribution between the forward and inversion models. To examine the behavior of the templated fracture inversion method under such situations, two models are developed for fracture characteristics inconsistent with the template. In the first model (Fig. 6(a)), the fracture extents and aperture distribution are the same as that in Fig. 4(a), but we use a uniform aperture template to image the non-uniform aperture distribution. In the second model (Fig. 6(b)), an irregular fracture shape is assumed in the forward model and we still use the elliptical template to image the fracture extents. The electric conductivity of rock formation σ_m is uniform with a value of 0.001 S/m.

As indicated by the inversion results, the fracture cannot be exactly imaged. However, the inversion results are still in good overall agreement with the actual fractures. Although there are some mismatches in fracture extents, most of the fracture areas in forward model are still correctly imaged, especially those with relative large aperture. In Fig. 6(a), the aperture from inversion is 2.22 × 10^{-3} m, which is

approximately equal to the average aperture in forward model (2.07×10^{-3} m). In Fig. 6(b), the aperture from inversion is 2.23×10^{-3} m, and the average aperture in forward model is 2.50×10^{-3} m.

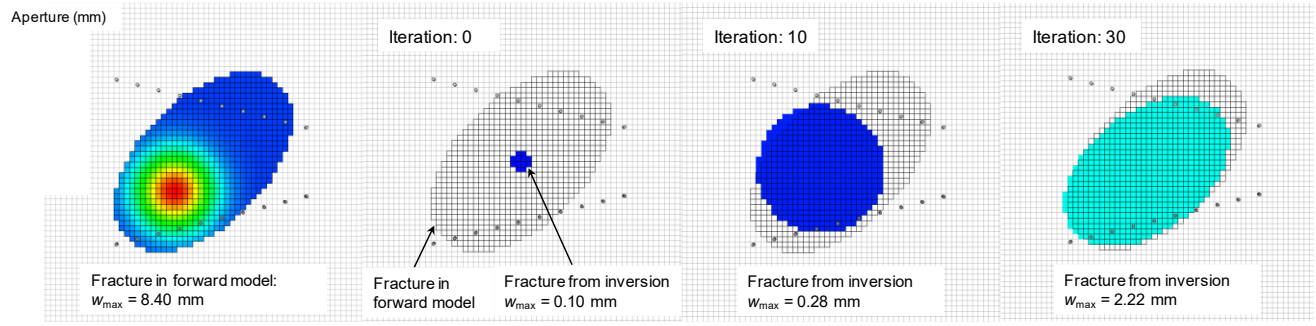

(a)

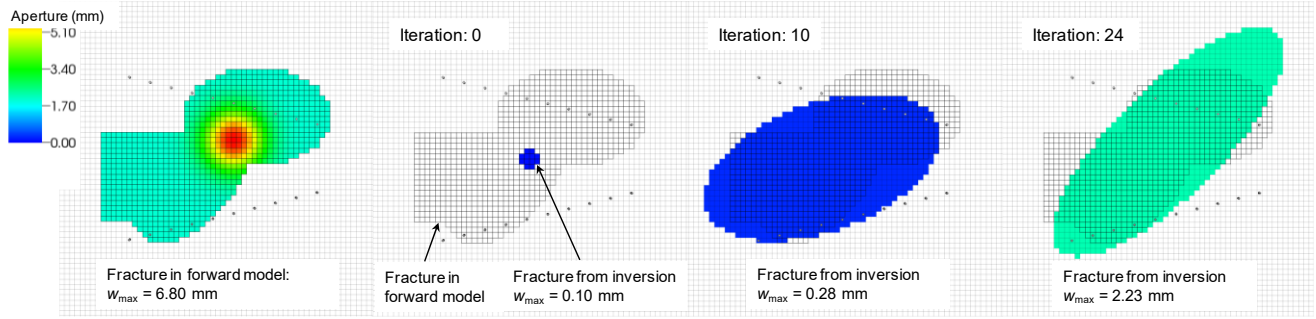

(b)

Figure 6: Imaging of hydraulic fracture with mismatch in fracture extents and aperture distribution. (a): The parameters describing the elliptical fracture in forward model are $x_0 = 0$ m, $y_0 = 0$ m, $a = 21.2$ m, $b = 12.7$ m, $\theta = 45.0°$, $\sigma_f = 1 \times 10^{-7}$ S/m. The parameters for the Gaussian function describing the aperture distribution are $n = 1$, $x_1 = (-5, -5, 0)$, $A_1 = 0.1$, $\varepsilon_1 = 5.0$, $w_0 = 0.5$ mm. The aperture distribution in the inversion model is uniform with an initial value of 0.1 mm; (b): The fracture shape in forward model is irregular and $\sigma_f = 1 \times 10^{-7}$ S/m. Parameters for the Gaussian function describing the aperture distribution are $n = 1$, $x_1 = (4, 4, 0)$, $A_1 = 0.05$, $\varepsilon_1 = 4.0$, $w_0 = 2$ mm. The aperture distribution in the inversion model is uniform with an initial value of 0.1 mm.

4. CONCLUSIONS

Compared with the traditional voxel-based, smoothness constrained inversion method, the templated fracture inversion method uses more *a priori* known information to regularize the imaging of hydraulic fracture and improve the inversion accuracy, both for fracture extents and aperture distribution. Different templates for fracture shape and aperture distribution can be employed to image different hydraulic fracture patterns. In this study, we use ellipses as the template for fracture extents and Gaussian function as the template to describe aperture distribution. Therefore, the variable space includes the five parameters describing the fracture extents (position of the fracture center x_0 and y_0, semi axis length a and b, rotation angle θ) and the $4n+1$ parameters describing the aperture distribution (n is the number of Gaussian functions used in the template for aperture distribution). For templated fracture inversion, the variable space is remarkably reduced compared to the smoothness constrained inversion, and therefore the method is more effective in imaging of hydraulic fracture.

ACKNOWLEDGEMENT

This material was based upon work supported by the U.S. Department of Energy, Office of Energy Efficiency and Renewable Energy (EERE), Office of Technology Development, Geothermal Technologies Office, under Award Number DE-AC52-07NA27344 with LLNL, Award Number DE-AC05-76RL01830 with PNNL, and Award Number DE-AC02-05CH11231 with LBNL. Publication releases for this manuscript are under LLNL-CONF-746206. The United States Government retains, and the publisher, by accepting the article for publication, acknowledges that the United States Government retains a non-exclusive, paid-up, irrevocable, world-wide license to publish or reproduce the published form of this manuscript, or allow others to do so, for United States Government purposes. The research supporting this work took place in whole or in part at the Sanford Underground Research Facility in Lead, South Dakota. The assistance of the Sanford Underground Research Facility and its personnel in providing physical access and general logistical and technical support is acknowledged.

REFERENCES

Bazin, S., Pfaffhuber, A.: Mapping of Quick Clay by Electrical Resistivity Tomography under Structural Constraint, *Journal of Applied Geophysics*, **98**, (2013), 280-287.

Bouchedda, A., Bernard, G., Gloaguen, E.: Constrained Electrical Resistivity Tomography Bayesian Inversion Using Inverse Matérn Covariance Matrix, *Geophysics*, **82**, (2017), 129-141.

Castillo, D., Hunterl, S., Harben, P., Wright, C., Conant, R., Davis, E.: Deep Hydraulic Fracture Imaging: Recent Advances in Tiltmeter Technologies, *International Journal of Rock Mechanics and Mining Sciences*, **34**, (1997), 047.

Coscia, I., Greenhalgh, S.A., Linde, N., Doetsch, J., Marescot, L., Gu, T., Vogt, T., Green, A.G.: 3D Crosshole ERT for Aquifer Characterization and Monitoring of Infiltrating River Water, *Geophysics*, **76**, (2011), 49-59.

Daily, W., Ramirez, A.L., LaBrecque, D.J., Nitao, J.: Electrical Resistivity Tomography of Vadose Water Movement, *Water Resources Research*, **28**, (1992), 1429-1442.

Daily, W., Ramirez, A.l., Binley, A., LaBrecque, D.: Electrical resistance Tomography - Theory and Practice, *SEG Investigations in Geophysics*, **13**, (2005), 525-550.

Davies, R.J., Mathias, S.A., Moss, J., Hustoft, S., Newport, L.: Hydraulic Fractures: How Far Can They Go? *Marine and Petroleum Geology*, **37**, (2012), 1-6.

Dey, A., Morrison, H.F.: Resistivity Modeling for Arbitrarily Shaped Three-Dimensional Structures, *Geophysics*, **44**, (1979), 753-780.

Doetsch, J., Linde, N., Binley, A.: Structural Joint Inversion of Time-lapse Crosshole ERT and GPR Traveltime Data. *Geophysical Research Letters*, **37**, (2010), 1-6.

Fisher, K., and Warpinski, N.: Hydraulic Fracture Height Growth: Real Data, *SPE Production & Operations*, **27**, (2012), 8-19.

Fu, P., Johnson, S.M., Carrigan. C.R.: An Explicitly Coupled Hydro-Geomechanical Model for Simulating Hydraulic Fracturing in Arbitrary Discrete Fracture Networks, *International Journal for Numerical and Analytical Methods in Geomechanics*, **37**, (2013), 2278-2300.

He, Y.Y., Zhang, B.P., Duan, Y.T., Xue, C.J., Yan, X., He, C., Hu, T.Y.: Numerical Simulation of Surface and Downhole Deformation Induced by Hydraulic Fracturing, *Applied Geopyhsics*, **11**, (2014), 63-72.

Huang, L.J., Chen, Y., Gao, K., Fu, P.C., Morris, J.P., Ajo-Franklin, J., Nakagawa, S.: Numerical Modeling of Seismic and Displacement-Based Monitoring for the EGS Collab Project, *Proceedings,* GRC Transaction, Salt Lake City, Utah (2017).

Johnson, T.C., Versteeg, R.J., Rockhold, M., Slater, L.D., Ntarlagiannis, D., Greenwood, W.J., Zachara, J.: Characterization of a Contaminated Wellfield Using 3D Electrical Resistivity Tomography Implemented with Geostatistical, Discontinuous Boundary, and Known Conductivity constraints, *Geophysics*, **77**, (2012), 85-96.

Knox, H., Fu, P.C., Morris, J.P., Guglielmi, Y., Vermeul, V., Ajo-Franklin, J., Strickland, C., Johnson, T., Cook, P., Herrick, C., Lee, M.: Fracture and Flow Designs for the Collab/SIGMA-V Project, *Proceedings,* GRC Transaction, Salt Lake City, Utah (2017).

LaBrecque, D.J., Morelli, G., Daily, W.D., Ramirez, A.L., Lundegard, P.: Occam's Inversion of 3-D ERT Data. In: Oristaglio, M., Spies, B. (Eds.), Three-dimensional Electromagnetics, Geophysical Development No. 7, 575-590.

LaBrecque, D.J., and Yang, X.: Difference Inversion of ERT Data: A Fast Inversion Method for 3-D In Situ Monitoring, *Journal of Environmental and Engineering Geophysics*, **6**, (2001), 83–89.

Lesur, V., Michel, C., Andre, S.: 2-D and 3-D Interpretation of Electrical Tomography Measurements, Part 2 : The Inverse Problem, *Geophysics*, **64**, (1999), 396-402.

Magnusdottir, L., Horne, R.N.: Characterization of Fractures in Geothermal Reservoirs using resistivity, *Proceedings,* Thirty-Sixth Workshop on Geothermal Reservoir Engineering, Stanford University, Stanford, CA (2010).

Maxwell, S.C., Urbancic, T.I., Steinsberger, N., Zinno, R.: Microseismic Imaging of Hydraulic Fracture Complexity in the Barnett Shale, *Proceedings,* SPE Annual Technical Conference and Exhibition, San Antonio, Texas (2002).

McClure, M.W., Horne, R.N.: An investigation of stimulation mechanisms in Enhanced Geothermal Systems, *International Journal of Rock Mechanics and Mining Sciences*, **72**, (2014), 242-260.

Niitsuma, H., and Saito, H.: Evaluation of the Three-dimensional Configuration of a Subsurface Artificial Fracture by the Triaxial Shear Shadow Method, *Geophysics*, **56**, (1991), 2118-2128.

Nimmer, R.E., Osiensky, J.L., Williams, B.C.: Electrical Resistivity Imaging of Conductive Plume Dilution in Fractured Rock, *Hydrogeology Journal*, **15**, (2007), 877-890.

Ramachandran, K., Tapp, B., Rigsby, T., Lewallen, E.: Imaging of Fault and Fracture Controls in the Arbuckle-Simpson Aquifer, Southern Oklahoma, USA, through Electrical Resistivity Sounding and Tomography Methods, International Journal of Geophysics, 2012, (2012), 184836.

Ramirez, A., Daily, W., LaBrecque, D., Owen, E., Chesnut, D.: Monitoring an Underground Steam Injection Process Using Electrical Resistance Tomography, *Water Resources Research*, **29**, (1993), 73-87.

Robert, T., Caterina, D., Deceuster, J., Kaufmann, O., Nguyen, F.: Case History: A Salt Tracer Test Monitored with Surface ERT to Detect Preferential Flow and Transport Paths in Fractured/Karstified Limestones, *Geophysics*, **77**, (2012), 55-67.

Robinson, J., Johnson, T., Slater, L.: Evaluation of Known-Boundary and Resistivity Constraints for Improving Cross-borehole DC Electrical Resistivity Imaging of Discrete Fractures, *Geophysics*, **78**, (2013), 115-127.

Robinson, J., Johnson, T., Slater, L.: Challenges and Opportunities for Fractured Rock Imaging Using 3D Cross-borehole Electrical Resistivity, *Geophysics*, **80**, (2015), 49-61.

Robinson, J., Slater, L., Johnson, T., Shapiro, A., Tiedeman, C., Ntarlagiannis, D., Johnson, C., Day-Lewis, F., Lacombe, P., Imbrigiotta, T., Lane, J.: Imaging Pathways in Fractured Rock Using Three-Dimensional Electrical Resistivity Tomography, *Groundwater*, **54**, (2016), 186-201.

Settgast, R.R., Fu, P.C., Walsh, S.D.C., White, J.A., Annavarapu, C., Ryerson. F.J.: A Fully Coupled Method for Massively Parallel Simulation of Hydraulically Driven Fractures in 3-Dimensions, *International Journal for Numerical and Analytical Methods in Geomechanics*, **41**, (2017), 627-653.

Slater, L., Binley, A.: Synthetic and Field-Based Electrical Imaging of a Zero-valent Iron Barrier: Implications for Monitoring Long-term Barrier Performance, *Geophysics*, **71**, (2006), 129-137.

Slater, L.D., Binley, A., Brown, D.: Electrical Imaging of Fractures Using Ground Water Salinity Change, *Ground Water*, **35**, (1997), 436-442.

Slater, L.D., and Sandberg, S.K.: Resistivity and Induced Polarization Monitoring of Salt Transport under Natural Hydraulic Gradients, *Geophysics*, **65**, (2000), 408-420.

Spitzer, K.: A 3-D Finite Difference Algorithm for DC Resistivity Modeling Using Conjugate Gradient Methods, *Geophysical Journal International,* 123, (1995), 903-914.

Trowbridge, S., Wicker, J., Courtier, J., Fairfield, R., Campbell, T.: Application of Microseismic to Assess Hydraulic Fracture Behavior in Relation to Completion Design and Landing Zone, *Proceedings,* Unconventional Resources Technology Conference, Austin, Texas (2017).

Vidic, R.D., Brantley, S.L., Vandenbossche, J.M., Yoxtheimer, D., Abad, J.D.: Impact of Shale Gas Development on Regional Water Quality, *Science*, **340**, (2013), 1235009.

Vinegar, H.J., Wills, P.B., Demartini, D.C., Shlyapobersky, J., Deeg, W.F.J., Adair, R.G., Woerpel, J.C., Fix, J.E., Sorrells, G.G.: Active and Passive Seismic Imaging of a Hydraulic Fracture in Diatomite, *Journal of Petroleum Technology*, **44**, (1992), 28-34.

Weiss, C.J., Aldridge, D.F., Knox, H.A., Schramm, K.A., Bartel, L.C.: The Direct-Current Response of Electrically Conducting Fractures Excited by a Grounded Current Source, *Geophysics*, **81**, (2016), 201-210.

Wills, P.B., DeMartini, D.C., Vinegar, H.J., Sjlyapobersk, J.: Active and Passive Imaging of Hydraulic Fractures, *The Leading Edge*, **11**, (1992), 15-22.

Wright, C.A., Conant, R.A., Golich, G.M., Bondor, P.L., Murer, A.S., Dobie, C.A.: Hydraulic Fracture Orientation and Production/Injection Induced Reservoir Stress Changes in Diatomite Waterfloods, *Proceedings,* SPE Western Regional Meeting, Bakersfield, CA (1995).

Yang, X.J., Chen, X., Carrigan, C.R., Ramirez, A.L.: Uncertainty Quantification of CO_2 Saturation Estimated from Electrical Resistance Tomography Data at the Cranfield Site, *International Journal of Greenhouse Gas Control*, **27**, (2014), 59–68.